

UGrid: An Efficient-And-Rigorous Neural Multigrid Solver for Linear PDEs

Anonymous Authors¹

Abstract

Numerical solvers of Partial Differential Equations (PDEs) are of fundamental significance to science and engineering. To date, the historical reliance on legacy techniques has circumscribed possible integration of big data knowledge and exhibits sub-optimal efficiency for certain PDE formulations, while data-driven neural methods typically lack mathematical guarantee of convergence and correctness. This paper articulates a mathematically rigorous neural solver for linear PDEs. The proposed ***UGrid*** solver, built upon the principled integration of ***U-Net*** and ***MultiGrid***, manifests a mathematically rigorous proof of both convergence and correctness, and showcases high numerical accuracy, as well as strong generalization power to various input geometry/values and multiple PDE formulations. In addition, we devise a new residual loss metric, which enables self-supervised training and affords more stability and a larger solution space over the legacy losses.

1. Introduction

Background and Major Challenges. PDEs are quintessential to various computational problems in science, engineering, and relevant applications in simulation, modeling, and scientific computing. Numerical solutions play an irreplaceable role in common practice because in rare cases do PDEs have analytic solutions, and many general-purpose numerical methods have been made available. Iterative solvers ((Saad, 2003)) are one of the most-frequently-used methods to obtain a numerical solution of a PDE. Combining iterative solvers with the multigrid method ((Briggs & McCormick, 2000)) significantly enhances the performance for large-scale problems. Yet, the historical reliance on legacy generic numerical solvers has circumscribed possible integration of big data knowledge and exhibits sub-optimal

efficiency for certain PDE formulations. In contrast, recent deep neural methods have the potential to learn such knowledge from big data and endow numerical solvers with compact structures and high efficiency, and have achieved impressive results ((Marwah et al., 2021)). However, many currently available neural methods treat deep networks as black boxes. Other neural methods are typically trained in a fully supervised manner on loss functions that directly compare the prediction and the ground truth solution, confining the solution space and resulting in numerical oscillations in the relative residual error even after convergence. These methods generally have challenges unconquered including, a lack of sound mathematical backbone, no guarantee of correctness or convergence, and low accuracy, thus unable to handle complex, unseen scenarios.

Motivation and Method Overview. Inspired by (Hsieh et al., 2019)'s prior work on integrating the structure of multigrid V-cycles ((Briggs & McCormick, 2000)) and U-Net ((Ronneberger et al., 2015)) with convergence guarantee, and to achieve high efficiency and strong robustness, we aim to fully realize neural methods' modeling and computational potential by implanting the legacy numerical methods' mathematical backbone into neural methods in this paper. In order to make our new framework fully explainable, we propose the UGrid framework (illustrated in Fig. 1) based on the structure of multigrid V-cycles for learning the functionality of multigrid solvers. We also improve the convolutional operators originating from (Hsieh et al., 2019) to incorporate arbitrary boundary conditions and multiple differential stencils without modifying the *overall structure* of the key iteration process, and transform the iterative update rules and the multigrid V-cycles into a concrete CNN structure.

Key Contributions. The salient contributions of this paper comprise: (1) *Theoretical insight*. We introduce a novel explainable neural PDE solver founded on a solid mathematical background, affording high efficiency, high accuracy, strong generalization power, and a mathematical guarantee to generalize to linear PDEs; (2) *New loss metric*. We propose a residual error metric as the loss function, which optimizes the residue of the prediction. Our newly-proposed error metric enables self-supervised learning and facilitates the unrestricted exploration of the solution space. Meanwhile, it eliminates the numerical oscillation on the relative residual error upon convergence, which has been frequently

¹Anonymous Institution, Anonymous City, Anonymous Region, Anonymous Country. Correspondence to: Anonymous Author <anon.email@domain.com>.

Preliminary work. Under review by the International Conference on Machine Learning (ICML). Do not distribute.

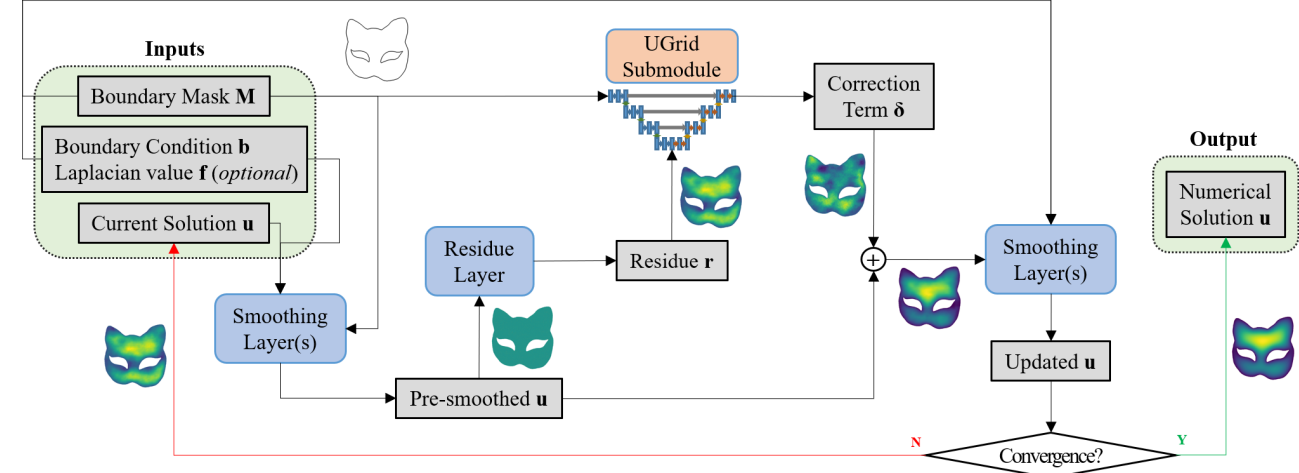


Figure 1. Overview of our novel method. Given PDE parameters and its current numerical estimation, the smoothing operations are applied multiple times first. Then, the current residue is fed into our UGrid submodule (together with the boundary mask). Next, the regressed correction term is applied and post-smoothed several times. Collectively, it comprises one iteration of the neural solver. The UGrid submodule (detailed in Fig. 2) aims to mimic the multigrid V-cycle, and its parameters are learnable, so as to endow our framework with the ability to learn from data.

observed on the legacy mean-relative-error-based loss metrics; and (3) *Extensive experiments*. We demonstrate our method’s capability to numerically solve PDEs by learning multigrid operators of various linear PDEs subject to arbitrary boundary conditions of complex geometries and topology, whose patterns are unseen during the training phase. Extensive experiments and comprehensive evaluations have verified all of our claimed advantages, and confirmed that our proposed method outperforms the SOTA.

2. Related Work

Black-box-like Neural PDE Solvers. Much research effort has been devoted to numerically solve PDEs with neural networks and deep learning techniques. However, most of the previous work treats neural networks as black boxes and thus come with no mathematical proof of convergence and correctness. As early as the 1990s, (Wang & Mendel, 1990a;b; 1991) applied simple neural networks to solve linear equations. Later, more effective neural-network-based methods like (Polycarpou & Ioannou, 1991; Cichocki & Unbehauen, 1992; Lagaris et al., 1998) were proposed to solve the Poisson equations. On the other hand, (Wu et al., 1994; Xia et al., 1999; Takala et al., 2003; Liao et al., 2010; Li et al., 2017) used Recurrent Neural Networks (RNNs) in solving systems of linear matrix equations. Most recently, the potential of CNNs and Generative Adversarial Networks (GANs) on solving PDEs was further explored by (Tompson et al., 2017; Tang et al., 2017; Farimani et al., 2017; Sharma et al., 2018; Özbay et al., 2021). Utilities used for neural PDE solvers also include backward stochastic differential

equations ((Han et al., 2018)) and PN junctions ((Zhang et al., 2019)). On the contrary, the proposed UGrid mimics the multigrid solver, and all its contents are explainable and have corresponding counterparts in an MG hierarchy.

Physics-informed Neural PDE Solvers. Physics-informed Neural Network (PINN)-based solvers effectively optimize the residual of the solution. Physics properties, including pressure, velocity ((Yang et al., 2016)) and non-locality ((Pang et al., 2020)) are also used to articulate neural solvers. Mathematical proofs on the minimax optimal bounds ((Lu et al., 2022)) and structural improvements ((Lu et al., 2021a;b)) are also made on the PINN architecture itself, endowing physics-informed neural PDE solvers with higher efficiency and interpretability. Hinted by these, we propose the residual loss metric, which enables self-supervised training, enlarges the solution space and enhances numerical stability.

Neural PDE Solvers with Mathematical Backbones. In 2009, (Zhou et al., 2009) proposed a NN-based linear system and its solving algorithm with a convergence guarantee. (Hsieh et al., 2019) modified the Jacobi iterative solver by predicting an additional correction term with a multigrid-inspired linear operator, and proposed a linear neural solver with guarantee on correctness upon convergence. (Greenfeld et al., 2019) proposed to learn a mapping from a family of PDEs to the optimal prolongation operator used in the multigrid Method, which is then extended to Algebraic Multigrids (AMGs) on non-square meshes via Graph Neural Networks (GNNs) by (Luz et al., 2020). On the other hand, (Li et al., 2021) proposed a Fourier neural operator

that learns mappings between function spaces by parameterizing the integral kernel directly in Fourier space. In theory, (Marwah et al., 2021) proved that when a PDE’s coefficients are representable by small NNs, the number of parameters needed will increase in a polynomial fashion with the input dimension.

3. Mathematical Preliminary

For mathematical completeness, we provide readers with a brief introduction to the concepts that are frequently seen in this paper.

Discretization of 2D Linear PDEs. A linear PDE with Dirichlet boundary condition could be discretized with finite differencing techniques ((Saad, 2003)), and could be expressed in the following form:

$$\begin{cases} \mathcal{D}u(x, y) = f(x, y), & (x, y) \in \mathcal{I} \\ u(x, y) = b(x, y), & (x, y) \in \mathcal{B} \end{cases}, \quad (1)$$

where \mathcal{D} is a 2D discrete linear differential operator, \mathcal{S} is the set of all points on the discrete grid, \mathcal{B} is the set of boundary points in the PDE, $\mathcal{I} = \mathcal{S} \setminus \mathcal{B}$ is the set of interior points in the PDE, $\partial\mathcal{S} \subseteq \mathcal{B}$ is the set of *trivial boundary points* of the grid.

Using \mathcal{D} ’s corresponding finite difference stencil, Eq. 1 can be formulated into a sparse linear system of size $n^2 \times n^2$:

$$\begin{cases} (\mathbf{I} - \mathbf{M})\mathbf{A}\mathbf{u} = (\mathbf{I} - \mathbf{M})\mathbf{f} \\ \mathbf{M}\mathbf{u} = \mathbf{M}\mathbf{b} \end{cases}, \quad (2)$$

where $\mathbf{A} \in \mathbb{R}^{n^2 \times n^2}$ is the 2D discrete differential operator, $\mathbf{u} \in \mathbb{R}^{n^2}$ encodes the function values of the interior points and the non-trivial boundary points; $\mathbf{f} \in \mathbb{R}^{n^2}$ encodes the corresponding partial derivatives of the interior points; $\mathbf{b} \in \mathbb{R}^{n^2}$ encodes the non-trivial boundary values; \mathbf{I} denotes the $n^2 \times n^2$ identity matrix; $\mathbf{M} \in \{0, 1\}^{n^2 \times n^2}$ is a diagonal binary boundary mask defined as

$$\mathbf{M}_{k,k} = \begin{cases} 1, & (i, j) \in \mathcal{B} \setminus \partial\mathcal{S} \\ 0, & (i, j) \in \mathcal{I} \end{cases}, \quad k = in + j, \quad 0 \leq i, j < n. \quad (3)$$

On the contrary of Eq. 1, both equations in Eq. 2 hold for *all* grid points.

Error Metric And Ground-truth Solution. When using numerical solvers, researchers typically substitute the boundary mask \mathbf{M} into the discrete differential matrix \mathbf{A} and the partial derivative vector \mathbf{f} , and re-formulate Eq. 2 into the following generic sparse linear system:

$$\tilde{\mathbf{A}}\mathbf{u} = \tilde{\mathbf{f}}. \quad (4)$$

The *residue* of a numerical solution \mathbf{u} is defined as

$$\mathbf{r}(\mathbf{u}) = \tilde{\mathbf{f}} - \tilde{\mathbf{A}}\mathbf{u}. \quad (5)$$

In the ideal case, the *absolute residual error* of an exact solution \mathbf{u}^* should be $r_{\mathbf{u}^*} = \|\mathbf{r}(\mathbf{u}^*)\| = 0$. However, in practice, a numerical solution \mathbf{u} could only be an approximation of the exact solution \mathbf{u}^* . The precision of \mathbf{u} is evaluated by its *relative residual error*, which is defined as

$$\varepsilon_{\mathbf{u}} = \left\| \tilde{\mathbf{f}} - \tilde{\mathbf{A}}\mathbf{u} \right\| / \left\| \tilde{\mathbf{f}} \right\|. \quad (6)$$

Typically, the ultimate goal of a numerical PDE solver is to seek the optimization of the relative residual error. If we have $\varepsilon_{\mathbf{u}} \leq \varepsilon_{\max}$ for some small ε_{\max} , we would consider \mathbf{u} to be a *ground-truth solution*.

Linear Iterator. A linear iterator (also called an iterative solver or a smoother) for generic linear systems like Eq. 4 could be expressed as

$$\mathbf{u}_{k+1} = \left(\mathbf{I} - \tilde{\mathbf{P}}^{-1} \tilde{\mathbf{A}} \right) \mathbf{u}_k + \tilde{\mathbf{P}}^{-1} \tilde{\mathbf{f}}, \quad (7)$$

where $\tilde{\mathbf{P}}^{-1}$ is an easily invertible approximation to the system matrix $\tilde{\mathbf{A}}$.

4. Novel Approach

The proposed UGrid neural solver is built upon the principled integration of the U-Net architecture and the Multigrid method. We observe that linear differential operators, as well as their approximate inverse in legacy iterative solvers, are analogous to convolution operators. E.g., the discrete Laplacian operator is a 3×3 convolution kernel. Furthermore, the multigrid V-cycle is also analogous to the U-Net architecture, with grid transfer operations mapped to up/downsampling layers. Moreover, the fine-tuning process of Multigrid’s critical components on specific PDE formulations could be completed by learning from big data. These technical observations lead to our neural implementation and optimization of the Multigrid routine.

In spite of high efficiency, generalization power remains a major challenge for neural methods. Many SOTA neural solvers, e.g., (Hsieh et al., 2019), fail to generalize to new scenarios unobserved during the training phase. Such new scenarios include: (i) New problem sizes; (ii) New, complex boundary conditions and right-hand sides, which includes geometries, topology, and values (noisy inputs). Moreover, some of these methods are tested on Poisson equations only; neither mathematical reasoning nor empirical results show that they could trivially generalize to other PDEs (with or without retraining). UGrid resolves all problems above.

UGrid is comprised of the following components: (1) The *fixed* neural smoother, which consists of our proposed convolutional operators (Sec. 4.1); (2) The *learnable* neural multigrid, which consists of our UGrid submodule (Sec. 4.2); (3) A residual loss metric (Sec. 4.3) which enables the self-supervised training process.

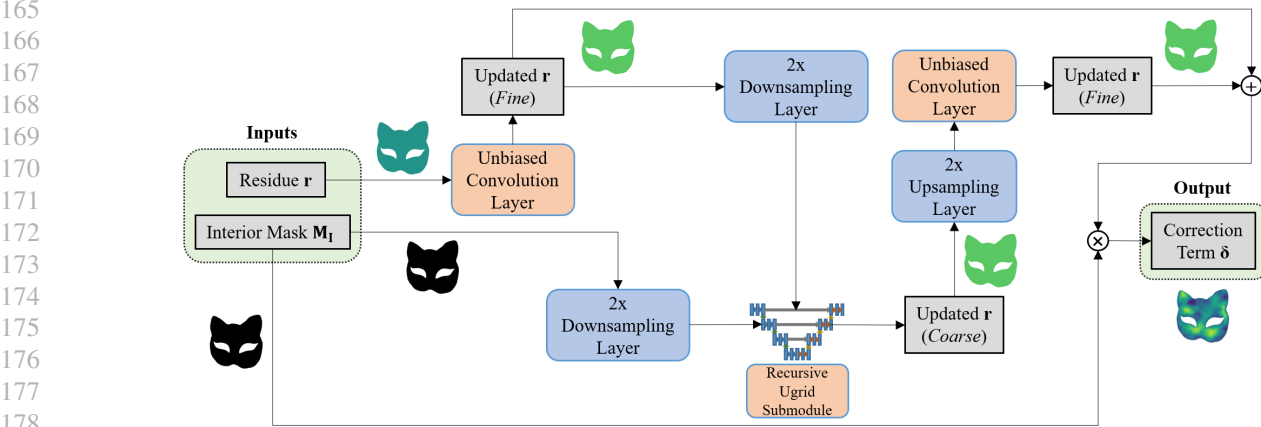


Figure 2. Overview of our recursive UGrid submodule. The residue is smoothed by *unbiased convolution layers*, downsampled to be *recursively updated* by a 2x-coarser UGrid submodule (note the orange recursive invocation of UGrid submodule on the bottom), then upsampled back to the fine grid, smoothed, and added with the initial residue by skip-connection. Boundary values are enforced by interior mask via element-wise multiplication. The convolution layers (shown in orange) are learnable; other layers (shown in blue) are the fixed mathematical backbone.

4.1. Convolutional Operators

This subsection is organized as follows: Sec. 4.1.1 introduces the masked operators, which mimic the smoothers in a legacy Multigrid routine; and Sec. 4.1.2 introduces the masked residual operators for residue calculation.

4.1.1. MASKED CONVOLUTIONAL ITERATOR

A trivial linear iterator in the form of Eq. 7 does **not** fit in a neural routine. This is because in practice, the system matrix \mathbf{A} for its corresponding differential operator encodes the *boundary geometry* and turns into matrix $\tilde{\mathbf{A}}$ in Eq. 4. $\tilde{\mathbf{A}}$'s elements are input-dependent, and is thus impossible to be expressed as a *fix-valued* convolution kernel.

We make use of the masked version of PDEs (Eq. 2) and their *masked convolutional iterators*, which are natural extensions of Eq. 7:

$$\mathbf{u}_{k+1} = (\mathbf{1} - \mathbf{M}) ((\mathbf{I} - \mathbf{P}^{-1} \mathbf{A}) \mathbf{u}_k + \mathbf{P}^{-1} \mathbf{f}) + \mathbf{M} \mathbf{b}, \quad (8)$$

where \mathbf{P}^{-1} is an easily-invertible approximation on the discrete differential operator \mathbf{A} . The correctness of Eq. 8 is guaranteed by the following Theorem (proved as Theorem A.3 in the supplemental materials):

Theorem 4.1. *For a PDE in the form of Eq. 2, the masked iterator Eq. 8 converges to its ground-truth solution when its prototype Jacobi iterator converges and \mathbf{P} is full-rank diagonal.*

Matrix \mathbf{A} has different formulations for different linear PDEs. Without loss of generality, we consider the following problem formulations. Other possible PDE formulations are essentially combinations of differential primitives available in the three problems below, and our convolutional

operators could be trivially extended to higher orders of differentiation.

2D Poisson Problem. Under Dirichlet boundary condition, a Poisson problem could be expressed as follows:

$$\begin{cases} \nabla^2 u(x, y) = f(x, y), & (x, y) \in \mathcal{I} \\ u(x, y) = b(x, y), & (x, y) \in \mathcal{B} \end{cases}, \quad (9)$$

where u is the unknown scalar field, f is the Laplacian field, and b is the Dirichlet boundary condition.

Matrix \mathbf{A} could be assembled by the five-point finite difference stencil for 2D Laplace operators ((Saad, 2003)), and we could simply let $\mathbf{P} = -4\mathbf{I}$, where \mathbf{I} denotes the identity matrix. The update rule specified in Eq. 8 thus becomes

$$\begin{aligned} \mathbf{u}_{k+1}(i, j) = & \frac{1}{4}(\mathbf{1} - \mathbf{M})(\mathbf{u}_k(i-1, j) + \mathbf{u}_k(i+1, j) \\ & + \mathbf{u}_k(i, j-1) + \mathbf{u}_k(i, j+1) - \mathbf{f}) + \mathbf{M} \mathbf{b}. \end{aligned} \quad (10)$$

To transform the masked iterator into a convolution layer, we reorganize the column vectors \mathbf{u} , \mathbf{b} , \mathbf{M} and \mathbf{f} into $n \times n$ matrices with their semantic meanings untouched. Then, the neural **smoother** could be expressed as

$$\begin{aligned} \mathbf{u}_{k+1} &= \text{smooth}(\mathbf{u}_k) \\ &= (\mathbf{1} - \mathbf{M})(\mathbf{u}_k * \mathbf{J} - 0.25 \mathbf{f}) + \mathbf{M} \mathbf{b}, \\ \mathbf{J} &= \begin{pmatrix} 0 & 0.25 & 0 \\ 0.25 & 0 & 0.25 \\ 0 & 0.25 & 0 \end{pmatrix}. \end{aligned} \quad (11)$$

2D Helmholtz Problem. Under Dirichlet boundary condition, an inhomogeneous Helmholtz equation with spatially-varying wavenumber may be expressed as follows:

$$\begin{cases} \nabla^2 u(x, y) + k^2(x, y)u(x, y) = f(x, y), & (x, y) \in \mathcal{I} \\ u(x, y) = b(x, y), & (x, y) \in \mathcal{B} \end{cases}, \quad (12)$$

where u is the unknown scalar field, k^2 is the spatially-varying wavenumber, f is the (non-zero) right hand side, and b is the Dirichlet boundary condition.

For our proposed UGrid solver, we could naturally extend Eq. 11 into the following form to incorporate Eq. 12:

$$\mathbf{u}_{k+1} = \frac{1}{4 - \mathbf{k}^2} (\mathbf{1} - \mathbf{M})(\mathbf{u}_k * 4\mathbf{J} - \mathbf{f}) + \mathbf{M}\mathbf{b}, \quad (13)$$

where all notations retain their meanings as in Eq. 11.

2D Steady-state Convection-diffusion-reaction Problem.

Under Dirichlet boundary condition, an inhomogeneous steady-state convection-diffusion-reaction equation may be expressed as follows:

$$\left\{ \begin{array}{ll} \mathbf{v}(x, y) \cdot \nabla u(x, y) - \alpha \nabla^2 u(x, y) + \beta u(x, y) = f(x, y), & (x, y) \in \mathcal{I} \\ u(x, y) = b(x, y), & (x, y) \in \mathcal{B} \end{array} \right. \quad (14)$$

where u is the unknown scalar field, $\mathbf{v} = (v_x, v_y)^\top$ is the vector velocity field, α, β are constants, f is the (non-zero) right-hand side, and b is the Dirichlet boundary condition.

For our proposed UGrid solver, we could naturally extend Eq. 11 into the following form to incorporate Eq. 14:

$$\begin{aligned} \mathbf{u}_{k+1} = & \frac{1}{4\alpha + \beta} (\mathbf{1} - \mathbf{M}) \\ & (\alpha \mathbf{u}_k * 4\mathbf{J} + \mathbf{v_x}(\mathbf{u}_k * \mathbf{J_x}) + \mathbf{v_y}(\mathbf{u}_k * \mathbf{J_y}) + \mathbf{f}) \\ & + \mathbf{Mb}, \end{aligned} \quad (15)$$

$$\mathbf{J}_x = \begin{pmatrix} 0 & 0 & 0 \\ 0.5 & 0 & -0.5 \\ 0 & 0 & 0 \end{pmatrix}, \quad \mathbf{J}_y = \begin{pmatrix} 0 & -0.5 & 0 \\ 0 & 0 & 0 \\ 0 & 0.5 & 0 \end{pmatrix},$$

where \mathbf{J}_x and \mathbf{J}_y are two convolution kernels introduced for the gradient operator in Eq. 14, and all notations retain their meanings as in Eq. 11.

4.1.2. CONVOLUTIONAL RESIDUAL OPERATOR

Except for the smoother, the Multigrid method also requires the calculation of the residue in each iteration step. In practice, the **residue operator** (Eq. 5) can also be seamlessly

implemented as a convolution layer. Because our masked iterator (Eq. 8) guarantees that \mathbf{u} satisfies $\mathbf{M}\mathbf{u} = \mathbf{M}\mathbf{b}$ at any iteration step, the residue operator for Poisson problems could be simplified into

$$\mathbf{r}(\mathbf{u}) = (\mathbf{1} - \mathbf{M})(\mathbf{f} - \mathbf{u} * \mathbf{L}), \quad \mathbf{L} = \begin{pmatrix} 0 & 1 & 0 \\ 1 & -4 & 1 \\ 0 & 1 & 0 \end{pmatrix}. \quad (16)$$

For Helmholtz problems, Eq. 16 could be naturally extended into

$$\mathbf{r}(\mathbf{u}) = (1 - M)(\mathbf{f} - \mathbf{u} * \mathbf{L} - k^2 \mathbf{u}), \quad (17)$$

where all notations retain their meanings as in Eq. 16.

For steady-state convection-diffusion-reaction problems, we could extend Eq. 16 into

$$\mathbf{r}(\mathbf{u}) = (\mathbf{1} - \mathbf{M})(\mathbf{f} + \mathbf{v_x}(\mathbf{u} * \mathbf{J_x}) + \mathbf{v_y}(\mathbf{u} * \mathbf{J_y}) + \alpha \mathbf{u} * \mathbf{L} - \beta \mathbf{u}), \quad (18)$$

where all notations retain their meanings as in Eq. 16.

4.2. Neural Network Design

UGrid Iteration. We design the iteration step of our neural iterator as a sequence of operations as follows (which is illustrated in Fig. 1):

$$\begin{aligned}
 \mathbf{u} &= \text{smooth}^{\nu_1}(\mathbf{u}) && \text{(Pre-smooth for } \nu_1 \text{ times);} \\
 \mathbf{r} &= \mathbf{r}(\mathbf{u}) && \text{(Calculate the current residue);} \\
 \delta &= \text{UGrid}(\mathbf{r}, \mathbf{1} - \mathbf{M}) && \text{(UGrid submodule recursion);} \\
 \mathbf{u} &= \mathbf{u} + \delta && \text{(Apply the correction term);} \\
 \mathbf{u} &= \text{smooth}^{\nu_2}(\mathbf{u}) && \text{(Post-smooth for } \nu_2 \text{ times).}
 \end{aligned} \tag{19}$$

The entire iteration process is specifically designed to emulate the multigrid iteration ((Saad, 2003)): We use the pre-smoothing and post-smoothing layers (as specified in Eq. 11) to eliminate the high-frequency modes in the residue r , and invoke the *UGrid submodule* to eliminate the low-frequency modes.

UGrid Submodule. Our UGrid submodule is also implemented as a fully-convolutional network, whose structure is highlighted in Fig. 2. The overall structure of UGrid is built upon the principled combination of U-Net ((Ronneberger et al., 2015)) and multigrid V-cycle, and could be considered a “V-cycle” with skip connections. Just like the multigrid method, our UGrid submodule is also invoked recursively, where each level of recursion would coarsen the mesh grid by 2x.

To approximate the linearity of the multigrid iteration (note that we are learning to invert a system matrix), we implement the smoothing layers in the legacy multigrid V-cycle

(not to be confused with the pre-smoother and the post-smoother in Eq. 19, which are *outside* of the V-cycle hierarchy) as learnable 2D convolution layers *without* any bias. For the same reason, and inspired by (Hsieh et al., 2019), we also drop many commonly seen neural layers which would introduce non-linearity, such as normalization layers and activation layers.

4.3. Loss Function Design

Legacy Loss Metric. We refer the equivalents of the mean relative error between the prediction and a ground-truth solution as the *legacy loss metric*. The following Theorem (proved in Sec. A.5) shows that though intuitive, the legacy loss is unstable:

Theorem 4.2. *When a neural network converges on a legacy loss metric such that its prediction \mathbf{x} satisfies $\mathcal{L}_{\text{legacy}}(\mathbf{x}, \mathbf{y}) = \text{mean}(|\mathbf{x} - \mathbf{y}| / |\mathbf{y}|) \leq l_{\max}$, where \mathbf{y} denotes the ground truth value, the upper and lower bounds of \mathbf{x} 's relative residual error are still dependent on the input.*

Theorem 4.2 explains our experimental observations that: (1) Optimizing the legacy loss metric does **not** increase the precision in terms of the relative residual error; (2) The legacy loss metric also restricts the solution space: A numerical solution with low relative residual error may have a large relative difference from the so-called “ground truth” value, and such valid solutions are *unnecessarily* rejected by the legacy loss metric.

Proposed Residual Loss Metric. To overcome the shortcomings of the legacy loss metric, we propose to optimize the neural solver directly to the residue in a self-supervised manner:

$$\mathcal{L}_{\mathbf{r}_{\text{abs}}}(\mathbf{x}) = \mathbb{E}_{\mathbf{x}}[\|(\mathbf{I} - \mathbf{M})(\mathbf{f} - \mathbf{A}\mathbf{x})\|_2]. \quad (20)$$

We have conducted ablation studies on our relative loss metric and the legacy loss (Sec. 5 and Sec. A.6). The results showcase that the proposed residual loss performs better than the legacy loss in terms of both efficiency and accuracy. Heuristically, the proposed residual loss metric is closer to the fundamental definition of the precision of a PDE's solution, and is more robust and stable, because upon convergence, it guarantees an input-independent final accuracy.

Moreover, the self-supervised training process endows our method with the following merits: (1) Easier data generation (compared to other neural routines which are trained on the legacy loss), and thus achieve better numerical performance; (2) For a specific PDE formulation, we could easily get a decent neural multigrid solver optimized for that specific formulation (which outperforms existing general-purpose legacy routines), simply by training UGrid on the data generated. On the contrary, fine-tuning legacy solvers is

a non-trivial task requiring a solid mathematical background as well as non-trivial programming effort.

5. Experiments and Evaluations

Experiments Overview. For each of the three PDEs mentioned in Sec. 4.1: (i) Poisson problem, (ii) inhomogeneous Helmholtz problem with varying wave numbers, and (iii) inhomogeneous steady-state diffusion-convection-reaction problem, we train one UGrid model specialized for its formulation. We apply our model and the baselines to the task of 2.5D freeform surface modeling. These surfaces are modeled by the three types of PDEs as 2D height fields, with non-trivial geometry/topology. Each surface is discretized into: (1) Large-scale problem: A linear system of size $1,050,625 \times 1,050,625$; and (2) Small-scale problem: A linear system of size $66,049 \times 66,049$. UGrid is trained **on the large scale only**. The small-scale problems are designed to evaluate UGrid's generalization power to new problem sizes, with results available in the appendix due to the page limit.

In addition, we have conducted an ablation study on the residual loss metric (v.s. legacy loss) as well as the UGrid architecture itself (v.s. vanilla U-Net).

Data Generation and Implementation Details. Our new neural PDE solver is trained in a self-supervised manner on the residual loss. Before training, we synthesized a dataset with 16000 ($\mathbf{M}, \mathbf{b}, \mathbf{f}$) pairs. For Helmholtz and diffusion problems, we further random-sample their unique coefficient fields (more details available in Sec. A.8 and Sec. A.9.) To examine the generalization power of UGrid, the geometries of boundary conditions in our training data are limited to “Donuts-like” shapes as shown in Fig. 3 (h). Moreover, all training data are restricted to zero \mathbf{f} -fields *only*, i.e., $\mathbf{f} \equiv \mathbf{0}$. Our UGrid model has 6 recursive Multigrid sub-modules. We train our model and perform all experiments on a personal computer with 64GB RAM, AMD Ryzen 9 3950x 16-core processor, and NVIDIA GeForce RTX 2080 Ti GPU. We train our model for 300 epochs with the Adam optimizer. The learning rate is initially set to 0.001, and decays by 0.1 for every 50 epochs. We initialize all learnable parameters with PyTorch's default initialization policy.

Experimental Results. We compare our model with two state-of-the-art legacy solvers, AMGCL ((Demidov, 2019)), and NVIDIA AmgX ((NVIDIA Developer, 2022)), as well as one SOTA neural solver proposed by (Hsieh et al., 2019).

Our testcases as shown in Fig. 3. These are all with complex geometry and topology, and **none** of which are present in the training data, except the geometry of Fig. 3 (h). Testcase(s) (a-f) examines the strong generation power and robustness of UGrid for irregular boundaries with complex geometries and topology **unobserved** during the training phase; (g) is

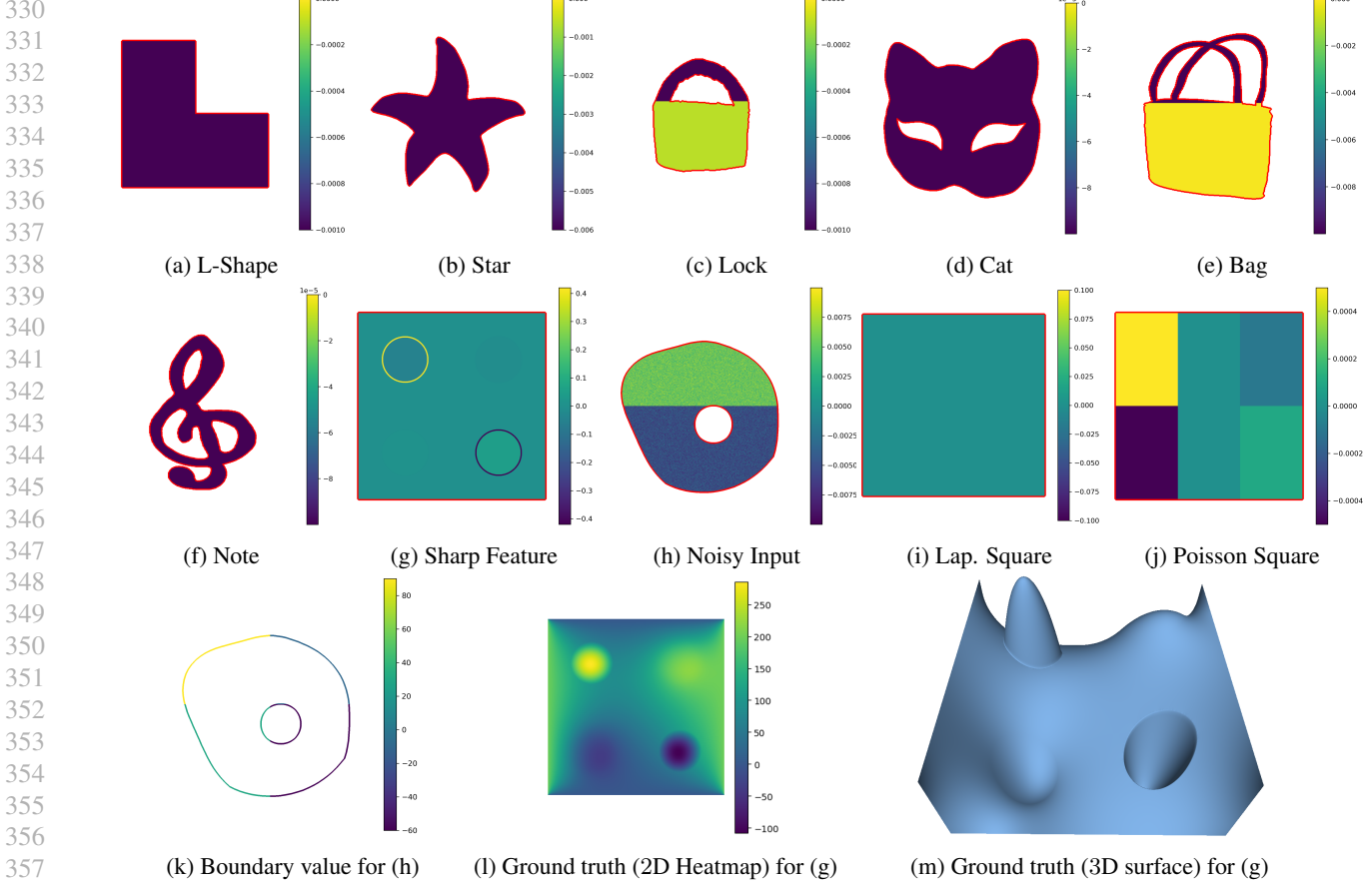


Figure 3. (a-j) illustrates the **f field distributions** of our testcases. The boundaries are shown in bold red lines for a better view. (k-m) are self-explanatory. The complete illustration of **boundary values** is available in Sec. A.2.

designed to showcase UGrid’s power to handle both sharp and smooth features in one scene (note that there are two sharp-feature circles on the top-left and bottom-right corners, as well as two smooth-feature circles on the opposite corners); (h) examines UGrid’s robustness against noisy input (boundary values, boundary geometries/topology, and Laplacian distribution); (i-j) are two baseline surfaces.

In Table 1, for Poisson problems, UGrid reaches the desirable precision 10-20x faster than AMGCL, 5-10x faster than NVIDIA AmgX, and 2-5x faster than (Hsieh et al., 2019) (note that (Hsieh et al., 2019) diverged for most of the testcases, those cases are not counted). This shows the efficiency and accuracy of our method. Moreover, the testcase “Noisy Input” showcases UGrid’s robustness. Furthermore, among all the ten testcases, only (the geometry of) the “Noisy Input” case is observed in the training phase of UGrid. This shows that UGrid converges to unseen scenarios whose boundary conditions are of complex geometry (e.g., “Cat”, “Star”, and “L-shape”) and topology (e.g., “Note”, “Bag”, and “Cat”). On the contrary, (Hsieh et al., 2019) failed to converge in most of our testcases, which

verifies one of their claimed limitations (i.e., no guarantee of convergence to unseen cases), and showcases the strong generalization power of our method. In addition, even for those converged cases, our method is still faster than (Hsieh et al., 2019).

In Table 2, for large-scale Helmholtz problems, UGrid reaches the desirable precision 7-20x faster than AMGCL and 5-10x faster than NVIDIA AmgX.

In Table 3, for large-scale steady-state diffusion-convection-reaction problems, UGrid reaches the desirable precision 2-12x faster than AMGCL and on average 2-6x faster than NVIDIA AmgX.

Ablation Study. The results are available in Table 4 (more details are available in Sec. A.6). The residual loss endows our UGrid model with as much as 2x speed up versus the legacy loss. The residual loss also endows UGrid to converge to the failure cases of its counterpart trained on legacy loss. These results demonstrate the claimed merits of the residual loss. On the other hand, it will diverge if we naively apply the vanilla U-Net architecture directly to

385
 386 *Table 1.* Qualitative results for large-scale Poisson problems. “Time” denotes the time (ms) to reach relative residual errors $\leq 10^{-4}$;
 387 “Error” denotes the final relative residual errors, divided by 10^{-5} . Convergence maps are also available in the supplemental materials.

Testcase	UGrid	AMGCL	AmgX	Hsieh et al.
L. Poisson	Time / Error	Time / Error	Time / Error	Time / Error
Bag	18.66 / 2.66	199.23 / 4.80	94.68 / 4.25	58.09 / 420
Cat	10.09 / 2.70	276.96 / 6.62	114.69 / 6.66	49.79 / 14.6
Lock	10.55 / 9.88	140.18 / 4.05	67.54 / 4.96	49.92 / 55.78
Noisy Input	10.16 / 2.64	262.06 / 3.52	116.91 / 9.19	51.07 / 2654
Note	10.31 / 4.06	127.28 / 3.00	64.35 / 4.56	20.26 / 8.67
Sharp Feature	20.01 / 3.80	422.49 / 4.14	176.34 / 3.87	51.22 / 24883
L-shape	15.26 / 8.43	221.87 / 6.74	110.07 / 4.89	50.53 / 96.1
Laplacian Square	15.10 / 3.88	422.13 / 3.63	188.98 / 9.76	31.43 / 9.03
Poisson Square	15.07 / 9.37	414.85 / 5.24	189.49 / 9.93	50.57 / 974
Star	15.18 / 7.50	152.83 / 6.65	72.90 / 5.29	50.45 / 384

403 *Table 2.* Qualitative results for large-scale Helmholtz problems.

Testcase	UGrid	AMGCL	AmgX
L. Helm.	Time / Error	Time / Error	Time / Error
Bag	20.03 / 8.08	203.71 / 5.69	94.00 / 6.24
Cat	16.85 / 0.51	278.07 / 7.26	119.16 / 3.26
Lock	12.83 / 6.82	144.10 / 4.24	70.71 / 5.16
N. Input	11.98 / 6.79	260.48 / 3.92	116.76 / 9.27
Note	12.18 / 6.48	131.58 / 3.02	94.47 / 4.73
S. Feat.	57.68 / 9.86	422.55 / 9.85	Diverge
L-shape	23.14 / 4.68	231.89 / 9.98	113.06 / 5.19
Lap. Squ.	44.91 / 9.98	419.92 / 5.81	188.47 / 7.64
P. Squ.	43.55 / 8.31	421.44 / 9.84	193.35 / 8.96
Star	15.18 / 7.50	154.81 / 7.63	72.24 / 5.31

404 *Table 3.* Qualitative results for large-scale steady-state diffusion-convection-reaction problems.

Testcase	UGrid	AMGCL	AmgX
L. Diff.	Time / Error	Time / Error	Time / Error
Bag	41.89 / 4.77	198.19 / 5.28	106.84 / 1.09
Cat	100.68 / 9.06	270.55 / 9.21	138.44 / 1.22
Lock	58.79 / 4.78	135.86 / 4.72	70.23 / 3.97
N. Input	84.29 / 8.75	256.90 / 4.40	122.29 / 0.08
Note	25.24 / 7.42	124.04 / 6.72	69.40 / 4.54
S. Feat.	33.80 / 7.90	407.64 / 4.25	191.97 / 0.46
L-shape	30.09 / 4.70	214.45 / 6.28	110.21 / 4.53
Lap. Squ.	60.31 / 6.62	409.15 / 4.56	198.03 / 7.50
P. Squ.	48.60 / 7.89	409.05 / 5.11	212.48 / 3.15
Star	25.59 / 9.38	147.47 / 6.01	71.75 / 4.16

418 Poisson’s equations. This showcases the significance of
 419 UGrid’s mathematically-rigorous network architecture.

423 *Table 4.* Ablation study on large-scale Poisson problems. Columns
 424 from left to right: UGrid trained with residual loss, UGrid trained
 425 with legacy loss, and vanilla U-Net trained with residual loss.

Testcase	UGrid	UGrid (L)	U-Net
L. Poi.	Time / Error	Time / Error	Time / Error
Bag	18.66 / 2.66	28.81 / 4.86	Diverge
Cat	10.09 / 2.70	23.80 / 1.43	Diverge
Lock	10.55 / 9.88	Diverge	Diverge
N. Input	10.16 / 2.64	20.65 / 2.42	Diverge
Note	10.31 / 4.06	Diverge	Diverge
S. Feat.	20.01 / 3.80	31.34 / 5.14	Diverge
L-shape	15.26 / 8.43	Diverge	Diverge
Lap. Squ.	15.10 / 3.88	30.72 / 2.76	Diverge
P. Squ.	15.07 / 9.37	31.52 / 3.33	Diverge
Star	15.18 / 7.50	Diverge	Diverge

426 **Limitations.** UGrid is currently designed for linear PDEs
 427 *only*, as Theorem 4.1 does not hold for non-linear PDEs.
 428 Another limitation lies in the fact that there is no mathematical
 429 guarantee on *how fast* UGrid will converge. As a
 430 consequence, UGrid does not necessarily converge faster on
 431 small-scale testcases.

6. Conclusion and Future Work

432 This paper has articulated a novel efficient-and-rigorous
 433 neural PDE solver built upon the U-Net and the Multigrid
 434 method, naturally combining the mathematical backbone
 435 of correctness and convergence as well as the knowledge
 436 gained from data observations. Extensive experiments validate
 437 all the claimed advantages of our proposed approach.
 438 Our future research efforts will be extending the current
 439 work to non-linear PDEs. The critical algorithmic barrier
 440 between our approach and non-linear PDEs is the limited
 441 expressiveness of the convolution semantics. We would like
 442 to explore more alternatives with stronger expressive power.

440 Potential Broader Impacts

441 Our work is completely theoretical and only involves the
 442 concept and the applications of partial differential equations.
 443 We believe our work has no potential impacts on the society.

445 References

446 Briggs, W. L. and McCormick, S. F. *A Multigrid Tutorial*.
 447 Society for Industrial and Applied Mathematics (SIAM),
 448 2000.

449 Cichocki, A. and Unbehauen, R. Neural Networks for Solving
 450 Systems of Linear Equations and Related Problems.
 451 *IEEE Transactions on Circuits and Systems I: Fundamental
 452 Theory and Applications*, 39(2):124–138, 1992.

453 Demidov, D. AMGCL: An Efficient, Flexible, and Extensible
 454 Algebraic Multigrid Implementation. *Lobachevskii Journal of Mathematics*, 455 40(5):535–546, 2019.

456 Demmel, J. W. *Applied Numerical Linear Algebra*. Society
 457 for Industrial and Applied Mathematics (SIAM), 1997.

458 Farimani, A. B., Gomes, J., and Pande, V. S. Deep
 459 Learning the Physics of Transport Phenomena. *CoRR*,
 460 abs/1709.02432, 2017.

461 Greenfeld, D., Galun, M., Kimmel, R., Yavneh, I., and Basri,
 462 R. Learning to Optimize Multigrid PDE Solvers. In *Proceedings of Machine
 463 Learning Research: International Conference on Machine Learning (ICML)*, volume 464 97, pp. 2415–2423, 2019.

465 Han, J., Jentzen, A., and E, W. Solving High-dimensional
 466 Partial Differential Equations using Deep Learning. *Proceedings of the National
 467 Academy of Sciences*, 115(34): 468 8505–8510, 2018. doi: 10.1073/pnas.1718942115.

469 Hsieh, J.-T., Zhao, S., Eismann, S., Mirabella, L., and Er-
 470 mon, S. Learning Neural PDE Solvers with Convergence
 471 Guarantees. In *International Conference on Learning
 472 Representations (ICLR)*, 2019.

473 Lagaris, I. E., Likas, A., and Fotiadis, D. I. Artificial Neural
 474 Networks for Solving Ordinary and Partial Differential
 475 Equations. *IEEE Transactions on Neural Networks and
 476 Learning Systems*, 9(5):987–1000, 1998.

477 Li, Z., Cheng, H., and Guo, H. General Recurrent Neural
 478 Network for Solving Generalized Linear Matrix Equation.
 479 *Complexity*, 2017:545–548, 2017.

480 Li, Z., Kovachki, N. B., Azizzadenesheli, K., Liu, B., Bhattacharya,
 481 K., Stuart, A., and Anandkumar, A. Fourier
 482 Neural Operator for Parametric Partial Differential Equations.
 483 In *International Conference on Learning Representations (ICLR)*, 2021.

484 Liao, W., Wang, J., and Wang, J. A Discrete-time Recurrent
 485 Neural Network for Solving Systems of Complex-valued
 486 Linear Equations. *International Conference in Swarm
 487 Intelligence (LCSI)*, 1(2):315–320, 2010.

488 Lu, L., Jin, P., Pang, G., Zhang, Z., and Karniadakis, G. E.
 489 Learning Nonlinear Operators via DeepONet Based on
 490 The Universal Approximation Theorem of Operators. *Nature
 491 Machine Intelligence*, 3(3):218–229, 2021a.

492 Lu, L., Meng, X., Mao, Z., and Karniadakis, G. E. Deep-
 493 XDE: A deep learning library for solving differential
 494 equations. *SIAM Review (SIREV)*, 63(1):208–228, 2021b.
 495 doi: 10.1137/19M1274067.

496 Lu, Y., Chen, H., Lu, J., Ying, L., and Blanchet, J. Machine
 497 Learning For Elliptic PDEs: Fast Rate Generalization
 498 Bound, Neural Scaling Law and Minimax Optimality. In
 499 *International Conference on Learning Representations
 500 (ICLR)*, 2022.

501 Luz, I., Galun, M., Maron, H., Basri, R., and Yavneh, I.
 502 Learning Algebraic Multigrid Using Graph Neural Networks.
 503 In *Proceedings of the 37th International Conference on
 504 Machine Learning (ICML)*, 2020.

505 Marwah, T., Lipton, Z., and Risteski, A. Parametric Com-
 506 plexity Bounds for Approximating PDEs with Neural
 507 Networks. In *Advances in Neural Information Processing
 508 Systems (NeurIPS)*, volume 34, pp. 15044–15055, 2021.

509 NVIDIA Developer. AmgX. <https://developer.nvidia.com/amgx>, 2022.

510 Pang, G., D’Elia, M., Parks, M., and Karniadakis, G.
 511 nPINNs: Nonlocal Physics-informed Neural Networks
 512 for a Parametrized Nonlocal Universal Laplacian Operator.
 513 Algorithms and Applications. *Journal of Computational
 514 Physics*, 422(5):109760, 2020.

515 Polycarpou, M. M. and Ioannou, P. A. A Neural-type Paral-
 516 lel Algorithm for Fast Matrix Inversion. *Proceedings of
 517 IEEE International Parallel and Distributed Processing
 518 Symposium (IPDPS)*, 5:108–113, 1991.

519 Ronneberger, O., Fischer, P., and Brox, T. U-Net: Convolu-
 520 tional Networks for Biomedical Image Segmentation. In
 521 *Medical Image Computing and Computer-Assisted Inter-
 522 vention (MICCAI)*, volume 9351, pp. 234–241, 2015.

523 Saad, Y. *Iterative Methods for Sparse Linear Systems*. So-
 524 ciety for Industrial and Applied Mathematics (SIAM),
 525 second edition, 2003.

526 Sharma, R., Farimani, A. B., Gomes, J., Eastman, P. K.,
 527 and Pande, V. S. Weakly-Supervised Deep Learning
 528 of Heat Transport via Physics Informed Loss. *CoRR*,
 529 abs/1807.11374, 2018.

- 495 Takala, J., Burian, A., and Ylinen, M. A Comparison of
 496 Recurrent Neural Networks for Inverting Matrices. *Proceedings of IEEE International Symposium on Signals,*
 497 *Circuits and Systems (ISSCS)*, 2:545–548, 2003.
- 498
- 500 Tang, W., Shan, T., Dang, X., Li, M., Yang, F., Xu, S., and
 501 Wu, J. Study on a Poisson’s Equation Solver based on
 502 Deep Learning Technique. In *IEEE Electrical Design of*
 503 *Advanced Packaging and Systems Symposium (EDAPS)*,
 504 volume 16, pp. 1–3, 2017.
- 505 Tompson, J., Schlachter, K., Sprechmann, P., and Perlin,
 506 K. Accelerating Eulerian Fluid Simulation with Con-
 507 volutional Networks. *Computer Animation and Virtual*
 508 *Worlds*, 70(3/4):3424–3433, 2017.
- 509
- 510 Wang, L. and Mendel, J. M. Structured Trainable Networks
 511 for Matrix Algebra. *Proceedings of International Joint*
 512 *Conference on Neural Networks (IJCNN)*, 2:125–132,
 513 1990a.
- 514
- 515 Wang, L. and Mendel, J. M. Three-Dimensional Structured
 516 Networks for Matrix Equation Solving. *IEEE Transac-*
 517 *tions on Computers*, 40(12):1337–1346, 1991.
- 518
- 519 Wang, L. X. and Mendel, J. M. Matrix Computations and
 520 Equation Solving using Structured Networks and Train-
 521 ing. *IEEE Conference on Decision and Control (CDC)*,
 522 40(12):1747–1750, 1990b.
- 523
- 524 Wu, G., Wang, J., and Hootman, J. A Recurrent Neural
 525 Network for Computing Pseudo-inverse Matrices. *Math-*
 526 *ematical and Computer Modelling*, 20(1):13–21, 1994.
- 527
- 528 Xia, Y., Wang, J., and Hung, D. L. Recurrent Neural
 529 Networks for Solving Linear Inequalities and Equations.
 530 *IEEE Transactions on Circuits and Systems I: Fundamen-*
 531 *tal Theory and Applications*, 46(4):452–462, 1999.
- 532
- 533 Yang, C., Yang, X., and Xiao, X. A Comparison of Recur-
 534 rent Neural Networks for Inverting Matrices. *Computer*
Animation and Virtual Worlds, 27(3/4):415–424, 2016.
- 535
- 536 Zhang, Z., Zhang, L., Sun, Z., Erickson, N., From, R., and
 537 Fan, J. Solving Poisson’s Equation using Deep Learn-
 538 ing in Particle Simulation of PN Junction. In *2019 Joint*
539 International Symposium on Electromagnetic Compati-
540 bility, Sapporo and Asia-Pacific International Sympo-
541 sium on Electromagnetic Compatibility (EMC Sapporo &
542 APEMC), pp. 305–308, 2019.
- 543
- 544 Zhou, Z., Chen, L., and Wan, L. Neural Network Algorithm
 545 for Solving System of Linear Equations. *Proceedings of*
546 International Conference on Computational Intelligence
and Natural Computing (ICCIC), 1:7–10, 2009.
- 547
- 548 Özbay, A. G., Hamzehloo, A., Laizet, S., Tzirakis, P., Rizos,
 549 G., and Schuller, B. Poisson CNN: Convolutional Neural

Networks for The Solution of The Poisson Equation on A
 Cartesian Mesh. *Data-Centric Engineering*, 2:e6, 2021.

A. Appendix

This supplemental material is provided to readers in the interest of our paper's theoretical and experimental completeness.

A.1. More Specifications on Our Training Data

UGrid is trained **only** with pairs of boundary masks and boundary values as shown in Fig. 4 (h). To be specific, throughout the whole training phase, UGrid is exposed only to *zero* f-fields and piecewise-constant Dirichlet boundary conditions with the “Donut-like” geometries. UGrid is **unaware** of all other complex geometries, topology, as well as the irregular/noisy distribution of boundary values/Laplacians observed in our testcases. This showcases the strong generalization power of our UGrid neural solver.

A.2. More Specifications on Our Testcases

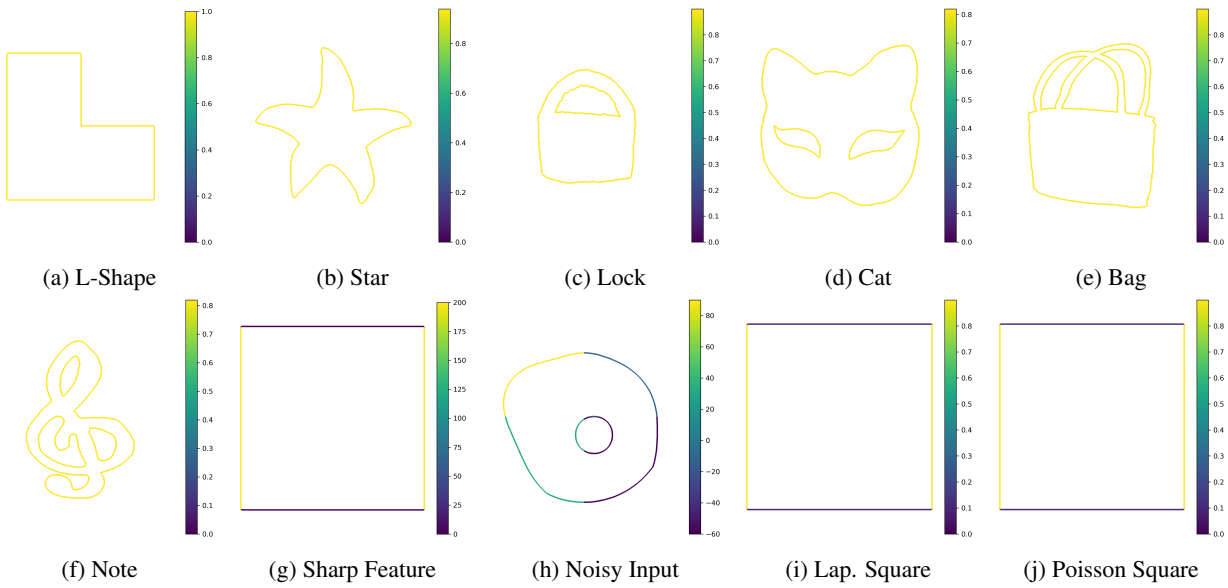


Figure 4. Illustration of the Dirichlet boundary values of our ten testcases. Again, all boundaries are shown in bold for a better view. Note that these boundaries are **not** required to be constant and could have *discontinuities*, which could be observed in testcases (g-j).

A.3. More Specifications on Our Qualitative Evaluations

Baseline Specifications. AMGCL is a C++ multigrid library with multiple GPU backends, we are comparing with its CUDA backend, with CG solver at the coarsest level. AmgX is part of NVIDIA’s CUDA-X GPU-Accelerated Library, and we adopt its official AMGX_LEGACY_CG configuration. (Hsieh et al., 2019)’s code is available at <https://github.com/ermongroup/Neural-PDE-Solver>. They did not release a pre-trained model, so we train their model with configurations as-is in their training and data-generation scripts, with minimal changes to make the program run.

Testing. All of our testcases are tested for 100 times and the results are averaged. For UGrid and (Hsieh et al., 2019), we set the maximum number of iterations as 64, and the iteration is terminated immediately upon reaching this threshold, no matter whether the current numerical solution has reached the desirable precision. AmgX has no direct support for relative residual errors, so we set tolerance on absolute residual errors case-by-case to achieve similar precision.

In our qualitative results, the “time” columns for AMGCL and AmgX include MG hierarchy building time and do not include training time for UGrid. This is because: (1) Training is required only once for one type of PDEs, and could be ignored over the solver’s lifespan; and (2) AMGCL/AmgX must reconstruct their MG hierarchy when input grid or boundary geometry changes; UGrid doesn’t need retraining for these cases. When MG hierarchy is constructed already, and only RHS changes, AMGCL/AmgX performs better. However, in fields like PDE-based CAD, grid and boundary-geometry changes as frequently as RHS, and UGrid will be a better choice.

Convergence Maps. For the experimental completeness of this paper, we also provide readers with the convergence maps of UGrid and the three SOTA solvers we compare with. The convergence maps are plotted for all of our ten testcases, each for its two different scales. We further plot these convergence maps as functions of time, and functions of iterations.

The convergence maps for large-scale problem are as follows:

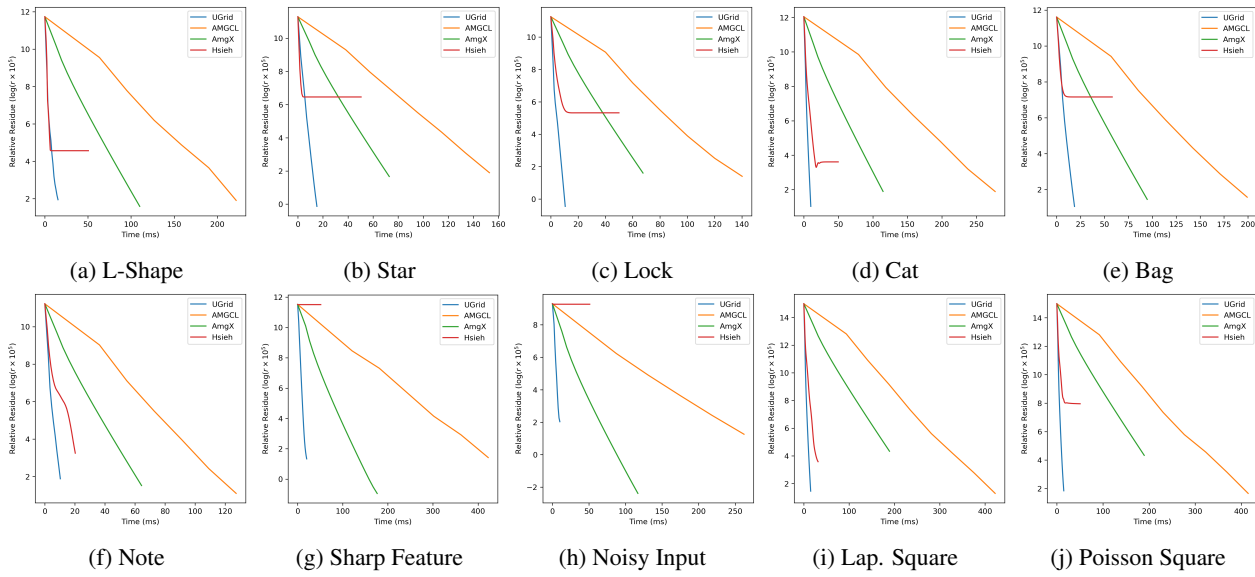


Figure 5. Convergence map on large-scale Poisson problem. The x coordinates are time(s), shown in ms; the y coordinates are the relative residual errors, shown in logarithm ($\log(r \times 10^5)$) for a better view.

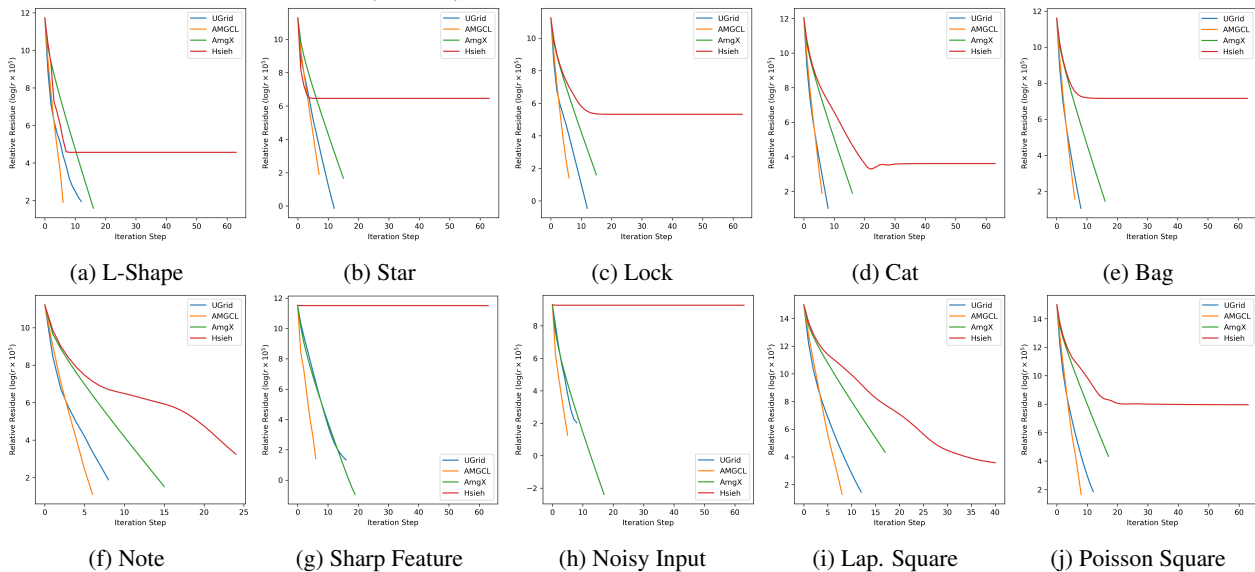


Figure 6. Convergence map on large-scale Poisson problem. The x coordinates are the iteration steps; the y coordinates are the relative residual errors, shown in logarithm ($\log(r \times 10^5)$) for a better view.

We also provide the convergence maps for small-scale problems as follows:

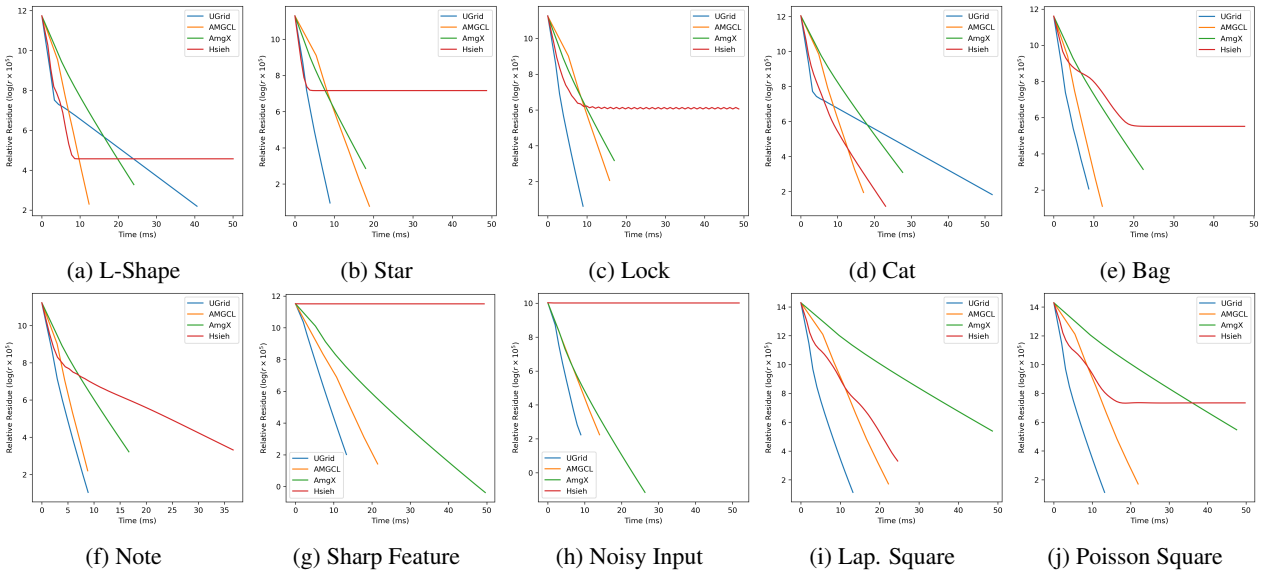


Figure 7. Convergence map on small-scale Poisson problem. The x coordinates are time(s), shown in ms; the y coordinates are the relative residual errors, shown in logarithm ($\log(r \times 10^5)$) for a better view.

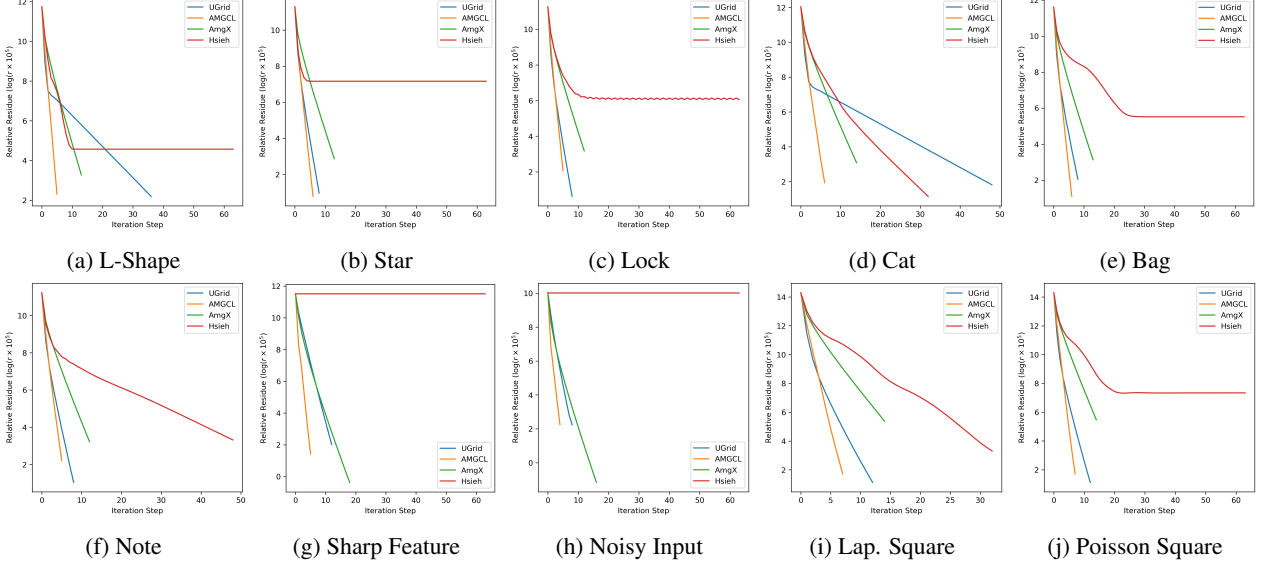


Figure 8. Convergence map on small-scale Poisson problem. The x coordinates are the iteration steps; the y coordinates are the relative residual errors, shown in logarithm ($\log(r \times 10^5)$) for a better view.

A.4. Proof of Correctness of Eq. 8

The proof of correctness of Eq. 8 originates from (Hsieh et al., 2019). For the completeness of this paper, we will also go through the mathematical proof. We start with the following Lemmas and Theorems:

Lemma A.1. *For a fixed linear iterator in the form of*

$$\mathbf{u}_{k+1} = \mathbf{G} \cdot \mathbf{u}_k + \mathbf{c}, \quad (21)$$

with a square update matrice \mathbf{G} having a spectral radius $\rho(\mathbf{G}) < 1$, $\mathbf{I} - \mathbf{G}$ is non-singular, and Eq. 21 converges for any constant \mathbf{c} and initial guess \mathbf{u}_0 . Conversely, if Eq. 21 converges for any \mathbf{c} and \mathbf{u}_0 , then $\rho(\mathbf{G}) < 1$.

715 *Proof.* Proved as Theorem 4.1 in (Saad, 2003). \square

716
717 **Lemma A.2.** For all operator norms $\|\cdot\|_k$, $k = 1, 2, \dots, \infty$, the spectral radius of a matrix \mathbf{G} satisfies $\rho(\mathbf{G}) \leq \|\mathbf{G}\|_k$.

718
719
720 *Proof.* Proved as Lemma 6.5 in (Demmel, 1997). \square

721
722 **Theorem A.3.** For a PDE in the form of Eq. 2, the masked iterator Eq. 8 converges to its ground-truth solution when its
723 prototype Jacobi iterator converges and \mathbf{P} is full-rank diagonal.

724
725 *Proof.* To prove this Theorem, we only need to prove: (1) Eq. 8 converges to a fixed point \mathbf{u} ; and (2) The fixed point \mathbf{u}
726 satisfies Eq. 2.

727 To prove (1), we only need to prove that for the update matrix

$$729 \quad 730 \quad \mathbf{G} = (\mathbf{I} - \mathbf{M})(\mathbf{I} - \mathbf{P}^{-1}\mathbf{A}),$$

731 its spectral radius $\rho(\mathbf{G}) < 1$. Given that the prototype Jacobi iterator converges, we have $\rho(\mathbf{I} - \mathbf{P}^{-1}\mathbf{A}) < 1$. From
732 Lemma A.2, taking the spectral norm $\|\cdot\|_2$ (i.e., $k = 2$), we have

$$733 \quad 734 \quad \rho(\mathbf{G}) \leq \|(\mathbf{I} - \mathbf{M})(\mathbf{I} - \mathbf{P}^{-1}\mathbf{A})\|_2 \leq \|\mathbf{I} - \mathbf{M}\|_2 \|\mathbf{I} - \mathbf{P}^{-1}\mathbf{A}\|_2.$$

735 Furthermore, because $\mathbf{I} - \mathbf{P}^{-1}\mathbf{A}$ is symmetric, we have $\rho(\mathbf{I} - \mathbf{P}^{-1}\mathbf{A}) = \|\mathbf{I} - \mathbf{P}^{-1}\mathbf{A}\|_2$. On the other hand, because
736 $\mathbf{I} - \mathbf{M} \in \{0, 1\}^{n^2 \times n^2}$ is a binary diagonal matrix, we have $\|\mathbf{I} - \mathbf{M}\|_2 = 1$. This yields $\rho(\mathbf{G}) < 1$.

737 To prove (2), we first notice that the fixed point $\mathbf{u} = \mathbf{u}_{k+1} = \mathbf{u}_k$ of Eq. 8 satisfies

$$741 \quad 742 \quad \mathbf{u} = (\mathbf{I} - \mathbf{M})((\mathbf{I} - \mathbf{P}^{-1}\mathbf{A})\mathbf{u} + \mathbf{P}^{-1}\mathbf{f}) + \mathbf{M}\mathbf{b}, \quad \text{i.e.,}$$

$$743 \quad 744 \quad (\mathbf{I} - \mathbf{M})\mathbf{u} + \mathbf{M}\mathbf{u} = (\mathbf{I} - \mathbf{M})((\mathbf{I} - \mathbf{P}^{-1}\mathbf{A})\mathbf{u} + \mathbf{P}^{-1}\mathbf{f}) + \mathbf{M}\mathbf{b}.$$

745 Again, since $\mathbf{M} \in \{0, 1\}^{n^2 \times n^2}$ is a binary diagonal matrix, we have

$$746 \quad \begin{cases} (\mathbf{I} - \mathbf{M})\mathbf{u} = (\mathbf{I} - \mathbf{M})((\mathbf{I} - \mathbf{P}^{-1}\mathbf{A})\mathbf{u} + \mathbf{P}^{-1}\mathbf{f}) \\ \mathbf{M}\mathbf{u} = \mathbf{M}\mathbf{b} \end{cases}. \quad (22)$$

747 The second equation in Eq. 22 is essentially the second equation in Eq. 2. Furthermore, the first equation in Eq. 22 could be
748 simplified into $(\mathbf{I} - \mathbf{M})\mathbf{P}^{-1}(\mathbf{A}\mathbf{u} - \mathbf{f}) = \mathbf{0}$. Since \mathbf{P} is full-rank diagonal, \mathbf{P}^{-1} should also be full-rank diagonal. Then we
749 have $(\mathbf{I} - \mathbf{M})(\mathbf{A}\mathbf{u} - \mathbf{f}) = \mathbf{0}$, which means that \mathbf{u} also satisfies the first equation in Eq. 2. \square

750 751 **A.5. Proof of Theorem. 4.2**

752 *Proof.* Denote $\varepsilon_{\mathbf{x}}$ as \mathbf{x} 's relative residual error, then we have:

$$753 \quad 754 \quad \varepsilon_{\mathbf{x}} = \frac{\|\tilde{\mathbf{f}} - \tilde{\mathbf{A}}\mathbf{x}\|}{\|\tilde{\mathbf{f}}\|} \approx \frac{\|\tilde{\mathbf{f}} - \tilde{\mathbf{A}}(\mathbf{y} \pm l_{\max}\mathbf{y})\|}{\|\tilde{\mathbf{f}}\|} = \frac{\|(\tilde{\mathbf{f}} - \tilde{\mathbf{A}}\mathbf{y}) \mp (l_{\max}\tilde{\mathbf{A}}\mathbf{y})\|}{\|\tilde{\mathbf{f}}\|}$$

$$755 \quad 756 \quad \leq \frac{\|\tilde{\mathbf{f}} - \tilde{\mathbf{A}}\mathbf{y}\|}{\|\tilde{\mathbf{f}}\|} + \frac{\|l_{\max}\tilde{\mathbf{A}}\mathbf{y}\|}{\|\tilde{\mathbf{f}}\|} = \varepsilon_{\mathbf{y}} + \frac{\|l_{\max}\tilde{\mathbf{A}}\mathbf{y}\|}{\|\tilde{\mathbf{f}}\|},$$

757 where $\varepsilon_{\mathbf{y}}$ denotes the relative residual error of the “ground-truth” value \mathbf{y} . $\varepsilon_{\mathbf{y}} \neq 0$ because in most cases, a PDE's
758 ground-truth solution could only be a numerical approximation with errors. The upper bound is input-dependent because $\tilde{\mathbf{A}}$
759 and $\tilde{\mathbf{f}}$ are input-dependent.

770 Similarly, we could prove that the lower bound of ε_x is also input-dependent:

$$\begin{aligned} \varepsilon_x &= \frac{\|\tilde{\mathbf{f}} - \tilde{\mathbf{A}}\mathbf{x}\|}{\|\tilde{\mathbf{f}}\|} \approx \frac{\|\tilde{\mathbf{f}} - \tilde{\mathbf{A}}(\mathbf{y} \pm l_{\max}\mathbf{y})\|}{\|\tilde{\mathbf{f}}\|} = \frac{\|\tilde{\mathbf{f}} - \tilde{\mathbf{A}}\mathbf{y}\| + \|l_{\max}\tilde{\mathbf{A}}\mathbf{y}\|}{\|\tilde{\mathbf{f}}\|} \\ &\geq \left| \frac{\|\tilde{\mathbf{f}} - \tilde{\mathbf{A}}\mathbf{y}\|}{\|\tilde{\mathbf{f}}\|} - \frac{\|l_{\max}\tilde{\mathbf{A}}\mathbf{y}\|}{\|\tilde{\mathbf{f}}\|} \right| = \left| \varepsilon_y - \frac{\|l_{\max}\tilde{\mathbf{A}}\mathbf{y}\|}{\|\tilde{\mathbf{f}}\|} \right| > 0. \end{aligned}$$

□

781 A.6. Ablation Study

783 For experimental completeness, we conduct ablation studies with respect to our residual loss and the UGrid architecture
 784 itself. In addition to the UGrid model trained with residual loss (as proposed in the main content), we also train another
 785 UGrid model with legacy loss, as well as one vanilla U-Net model with residual loss. This U-Net model has the same
 786 number of layers as UGrid, and has non-linear layers as proposed in (Ronneberger et al., 2015). We let the U-Net directly
 787 regress the solutions to Poisson’s equations. All these models are trained with the same data in the same manner (except for
 788 the loss metric), as detailed in Section 5.

789 We conduct qualitative experiments on the same set of testcases as detailed in Section 5, and the results are as follows:

790 In Table 5, the residual loss endows our UGrid model with as much as 2x speed up versus the legacy loss. The residual loss
 791 also endows UGrid to converge to the failure cases of its counterpart trained on legacy loss. These results demonstrate the
 792 claimed merits of the residual loss. On the other hand, it will **diverge** if we naively apply the vanilla U-Net architecture
 793 directly to Poisson’s equations. For experimental completeness only, we list the diverged results in the last column. (The
 794 “time” column measures the time taken for 64 iterations; the iterators are shut down once they reach this threshold.) This
 795 showcases the significance of UGrid’s mathematically-rigorous network architecture.

796 *Table 5.* Ablation study on large-scale Poisson problems.

Testcase	UGrid	UGrid (L)	U-Net
Large-scale	Time / Error	Time / Error	Time / Error
Bag	18.66 / 2.66	28.81 / 4.86	81.71 / 1384131
Cat	10.09 / 2.70	23.80 / 1.43	70.09 / 2539002
Lock	10.55 / 9.88	Diverge	70.92 / 1040837
N. Input	10.16 / 2.64	20.65 / 2.42	73.05 / 21677
Note	10.31 / 4.06	Diverge	69.97 / 614779
S. Feat.	20.01 / 3.80	31.34 / 5.14	70.08 / 222020
L-shape	15.26 / 8.43	Diverge	74.67 / 1800815
Lap. Squ.	15.10 / 3.88	30.72 / 2.76	72.24 / 30793035
P. Squ.	15.07 / 9.37	31.52 / 3.33	71.74 / 31043896
Star	15.18 / 7.50	Diverge	70.01 / 1138821

813 In Table 6, for small-scale problems, the residual loss still endows UGrid with as much as 2x speedup and stronger
 814 generalization power against its counterpart trained with legacy loss. Once again, the vanilla U-Net model diverged for all
 815 testcases, and we list its diverged results for experimental completeness only.

816 A.7. Qualitative Evaluations on Small-scale Poisson Problems

817 In Table 7, even on small-scale problems that hinder our solver with a compact multigrid-like hierarchy from delivering its
 818 full power, the UGrid model is still faster than or exhibits comparable efficiency with respect to the three SOTA legacy/neural
 819 solvers. Again, this shows the high efficiency as well as the strong generalization power of our new method. The testcases
 820 “Cat” and “L-shape” showcase that the generalization power (in terms of problem size) does come with a price of potentially
 821

Table 6. Comparison of UGrid with residual loss, UGrid with legacy loss (UGrid (L)), and U-Net with residual loss, on small-scale problems. “Time” denotes the time (ms) to reach relative residual errors $\leq 10^{-4}$ or for 64 iterations, whichever comes first; “Error” denotes the final relative residual errors, divided by 10^{-5} .

Testcase Small-scale	UGrid	UGrid (L)	U-Net
	Time / Error	Time / Error	Time / Error
Bag	8.76 / 8.05	17.89 / 4.50	71.86 / 678141
Cat	51.96 / 6.21	Diverge	68.89 / 1317465
Lock	9.00 / 2.11	18.32 / 2.83	69.47 / 189412
Noisy Input	8.94 / 6.00	17.88 / 6.58	69.54 / 21666
Note	8.87 / 2.75	17.79 / 3.06	69.59 / 24715
Sharp Feature	13.31 / 7.52	26.64 / 1.91	70.57 / 191499
L-shape	40.60 / 7.09	Diverge	69.71 / 1011364
Laplacian Square	13.21 / 3.27	22.23 / 9.55	73.80 / 15793109
Poisson Square	13.21 / 2.88	22.13 / 9.76	71.56 / 15393069
Star	8.92 / 2.36	17.60 / 5.69	73.72 / 502993

Table 7. Comparison of UGrid and state-of-the-art on small-scale Poisson problems.

Testcase S. Poisson	UGrid	AMGCL	AmgX	Hsieh et al.
	Time / Error	Time / Error	Time / Error	Time / Error
Bag	8.76 / 8.05	12.14 / 3.00	22.34 / 8.20	47.69 / 252
Cat	51.96 / 6.21	17.03 / 6.98	27.66 / 4.83	23.02 / 9.95
Lock	9.00 / 2.11	15.77 / 7.89	16.96 / 9.36	48.72 / 117.9
Noisy Input	8.94 / 6.00	14.00 / 9.39	26.30 / 3.14	51.79 / 5576
Note	8.87 / 2.75	8.79 / 9.02	16.68 / 7.23	36.66 / 8.28
Sharp Feature	13.31 / 7.52	21.47 / 4.15	49.59 / 6.85	49.31 / 24876
L-shape	40.60 / 7.09	12.36 / 9.97	24.08 / 9.35	50.06 / 96.44
Laplacian Square	13.21 / 3.27	22.22 / 5.60	48.60 / 3.98	24.57 / 6.54
Poisson Square	13.21 / 2.88	21.93 / 5.51	47.56 / 4.03	49.77 / 473
Star	8.92 / 2.36	18.93 / 2.17	17.96 / 9.42	48.68 / 456

downgraded efficiency. Thus, for the sake of the best efficiency, we still recommend re-training UGrid for problems of different sizes.

A.8. Specifications on Evaluations of Inhomogeneous Helmholtz Problems with Spatially-varying Wavenumbers

We train UGrid with the same training data and residual loss as mentioned in Section 5. As one exception, we also input randomly-sampled k^2 during training, evaluation, and testing. The randomly-sampled k^2 s used for training are illustrated in Fig. 9 (h).

For qualitative experiments, we use the same boundary conditions and Laplacian distributions as shown in Fig. 4 and Fig. 3, and we randomly initialize the wavenumber field k^2 across the whole domain, resulting in a noisy distribution:

The qualitative results for large-scale problems are available in the main paper as Table. 2.

In Table 8, even on small-scale problems that hinder our solver with a compact multigrid-like hierarchy from delivering its full power, UGrid is still faster than or exhibits comparable efficiency with respect to the SOTA.

A.9. Specifications on Evaluations of Inhomogeneous Steady-state Convection-diffusion-reaction Problems

We train UGrid in the same manner as for Helmholtz equations. As one exception, we input randomly-sampled \mathbf{v} s, α s, and β s during training, evaluation, and testing. These values are sampled using the same routine as for Helmholtz equations, resulting in noisy velocity fields like Fig. 9 as well as randomized α , β coefficients ($4\alpha + \beta \neq 0$). The qualitative results for large-scale problems are available in the main paper as Table. 3. Results for the small-scale problem are as follows:

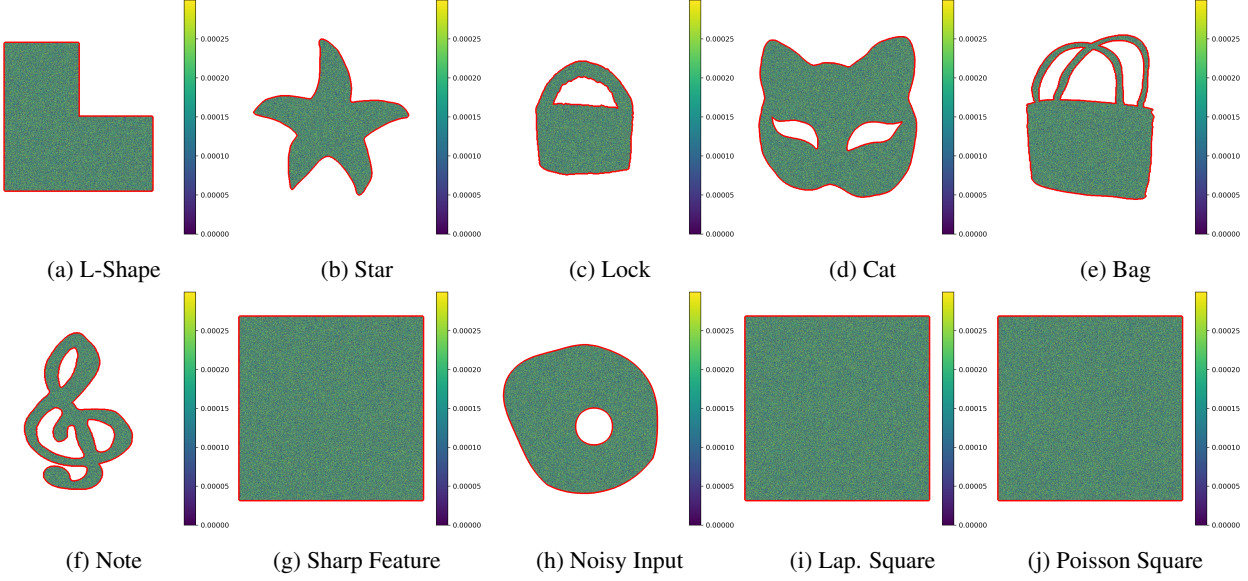


Figure 9. Illustration of the wavenumber distributions of our testcases. The boundaries are shown in bold red lines for a better view. (Boundary values are shown in Fig. 4.)

Table 8. Qualitative results for small-scale Helmholtz problems.

Testcase S. Helmholtz	UGrid Time / Error	AMGCL Time / Error	AmgX Time / Error
Bag	14.70 / 6.29	12.92 / 3.00	25.82 / 1.79
Cat	16.63 / 7.86	16.82 / 6.98	28.37 / 3.03
Lock	9.78 / 5.87	16.23 / 7.88	19.75 / 2.02
Noisy Input	14.95 / 0.76	14.34 / 9.40	28.92 / 0.04
Note	14.37 / 8.28	9.01 / 9.02	18.76 / 2.55
Sharp Feature	19.46 / 1.18	21.37 / 4.21	52.82 / 0.13
L-shape	14.64 / 0.88	12.29 / 9.99	26.90 / 2.10
Laplacian Square	14.60 / 4.60	22.43 / 5.59	43.68 / 17.8
Poisson Square	15.27 / 6.53	22.35 / 5.50	43.57 / 17.2
Star	9.77 / 5.96	19.09 / 2.16	20.89 / 2.18

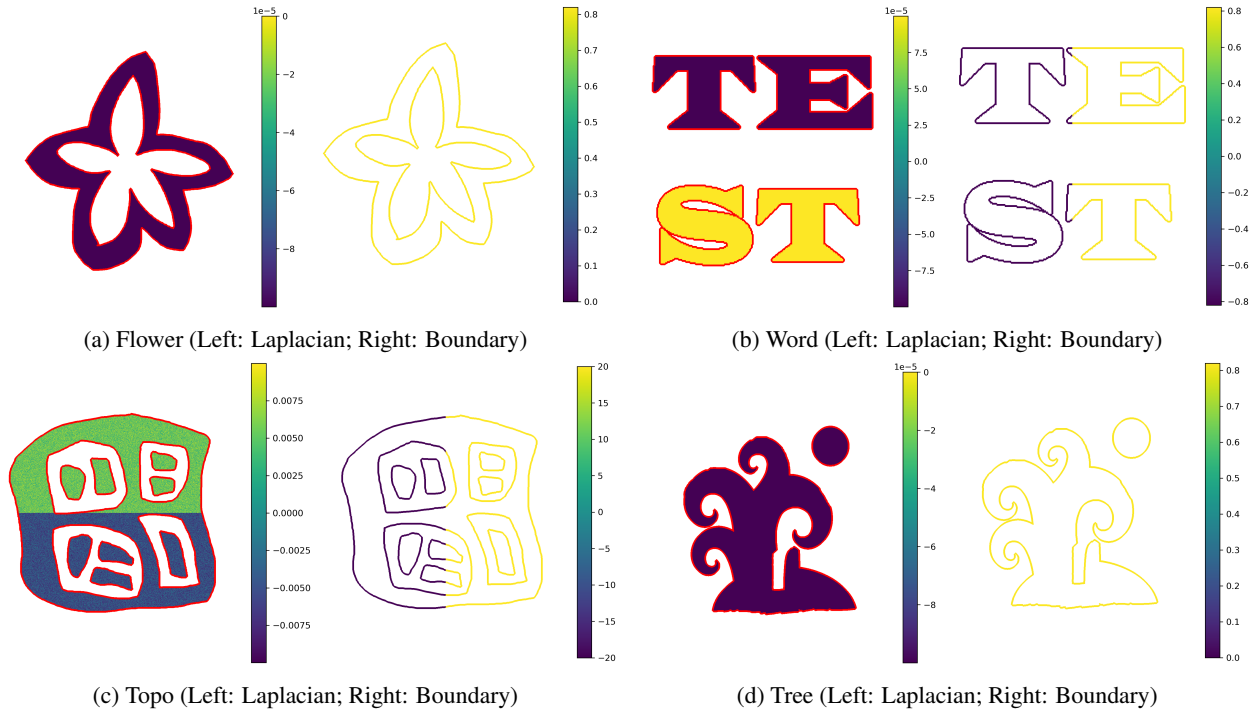
In Table 9, again, even on small-scale problems that hinder our solver with a compact multigrid-like hierarchy from delivering its full power, UGrid is still exhibits comparable efficiency with respect to the SOTA. This demonstrates UGrid's generalization power over problem sizes, though possibly at the price of relatively lower efficiency compared to the size it is trained on.

935
936
937
938
939
940
941
942
943
944
945
946
947
948
949
950
951
952
953
954
955
956
957
958
959
960
961
962
963
964
965
966
967
968
969
970
971
972
973
974
975
976
977
978
979
980
981
982
983
984
985
986
987
988
989**Table 9.** Qualitative results for small-scale Diffusion problems.

Testcase	UGrid	AMGCL	AmgX
S. Diffusion	Time / Error	Time / Error	Time / Error
Bag	16.99 / 3.79	12.34 / 9.94	22.58 / 3.66
Cat	69.12 / 8.76	16.57 / 9.79	27.44 / 6.74
Lock	17.07 / 1.43	16.07 / 6.34	18.34 / 4.06
Noisy Input	22.84 / 6.47	15.94 / 2.74	24.35 / 0.42
Note	22.76 / 1.17	9.38 / 2.67	19.25 / 3.79
Sharp Feature	17.05 / 5.15	21.41 / 4.29	41.67 / 0.72
L-shape	35.18 / 6.25	13.02 / 2.30	25.51 / 3.97
Laplacian Square	90.73 / 64.5	22.14 / 8.17	50.49 / 3.50
Poisson Square	50.95 / 5.01	22.05 / 7.34	50.06 / 3.28
Star	17.06 / 3.69	18.70 / 7.55	18.88 / 4.71

A.10. Additional Experiments for Rebuttal

We have conducted four additional experiments to showcase the generalization power of the proposed UGrid solver. The four testcases are illustrated as follows:

**Figure 10.** Illustration of four additional testcases.

990 The qualitative results are as follows:

991
992
993 *Table 10.* Qualitative results for additional large-scale Poisson problems. “Time” denotes the total time (ms) to reach relative residual
994 errors $\leq 10^{-4}$, and “Assembly” and “Iteration” denotes time (ms) for the two phases for AMG solvers; “Error” denotes the final relative
995 residual errors, divided by 10^{-5} .

996 Testcase	997 UGrid	998 AMGCL	999 AmgX	1000 Hsieh et al.
L. Poisson	Time / Error	Time / Assembly / Iteration / Error	Time / Assembly / Iteration / Error	Time / Error
Flower	18.52 / 1.60	144.91 / 138.00 / 6.91 / 3.07	69.14 / 18.11 / 51.03 / 5.41	27.23 / 7.16
Word	41.14 / 5.60	188.59 / 178.34 / 10.25 / 4.15	108.51 / 21.44 / 87.06 / 4.62	50.76 / 2612
Topo	10.30 / 4.29	210.06 / 203.86 / 6.20 / 4.86	97.22 / 24.29 / 72.93 / 2.94	52.29 / 3933
Tree	10.05 / 2.52	173.70 / 166.86 / 6.84 / 4.61	78.73 / 20.98 / 57.76 / 6.88	16.05 / 7.60

1003 In Table 10, UGrid still delivers similar efficiency, accuracy and generalization power like the ten testcases covered in the
1004 main contents of the manuscript. Note that Hsieh et al. **diverged** for testcases “Word” and ”Topo”; their time for these two
1005 cases is the time to reach the maximum number of iterations.